

Hierarchical 3D Cuprous Sulfide Nanoporous Cluster Arrays Self-Assembled on Copper Foam as a Binder-Free Cathode for Hybrid Magnesium-Based Batteries

Guilei Zhu, Guanglin Xia, and Xuebin Yu*

On account of easy accessibility, high theoretical volumetric capacity and dendrite-free magnesium (Mg) anode, Mg battery has a great promise to be next generation rechargeable batteries, yet still remains a challenging task in acquiring fast Mg^{2+} kinetics and effective cathode materials. Herein, hierarchical 3D cuprous sulfide porous nanosheet decorated nanowire cluster arrays with robust adhesion on copper foam (Cu_2S HP/CF), which is employed as a binder-free conversion cathode material for magnesium/lithium hybrid battery, delivering impressively initial and reversible specific capacity of 383 and 311 mAh g^{-1} at 100 mA g^{-1} , respectively, which are obviously outperformed corresponding powder cathode in a traditional method by using polymer binder, is reported. Intriguingly, benefiting from the hierarchical nanoporous array architecture and self-assembly feature, Cu_2S HP/CF cathode shows a remarkable cycling stability with a high capacity of 129 mAh g^{-1} at 300 mA g^{-1} over 500 cycles. This work not only highlights a guide for designing hierarchical nanoporous materials derived from metal-organic frameworks, but also provides a novel strategy of in situ formation to fabricate binder-free cathodes.

Magnesium (Mg) ion batteries (MIBs) are rising as an intriguing stationary energy storage because of the advantages of Mg anode. To be more specific, Mg metal as two-charge carrier excels at its high volumetric capacity (3833 mAh cm^{-3} ; 2046 mAh cm^{-3} for Li), dendrite-free deposition, handling safety, and high natural resources.^[3] However, the development of MIBs is curbed by the sluggish Mg^{2+} kinetics and the lack of suitable cathode materials. In recent years, given that the cells can be an integration of safe and inexpensive Mg anode and fast and highly reversible Li^+ transportation, hybrid $\text{Mg}^{2+}/\text{Li}^+$ batteries (MLIBs) have made a splash. Moreover, compared to salt-analogs of LIBs ($\text{Mg}(\text{PF}_6)_2$, $\text{Mg}(\text{TFSI})_2$, and $\text{Mg}(\text{ClO}_4)_2$), all-phenyl complex (APC), which is one of the most representative complex electrolytes, is of great benefit for vastly enhanced kinetics and reversibility via bringing in an additional

1. Introduction


The immense appeal of rechargeable battery system has spurred a boom to probe various kinds of metal-ion batteries since we have to vigorously promote sustainable energy and carbon-free transportation due to energy crisis and environmental concerns.^[1,2] To date, lithium (Li) ion batteries (LIBs) with the merits of high energy density and outstanding cycling life are deemed to be the most successful and convenient energy storage device, and serve as an obligato part in our daily life. Unfortunately, the ever-increasing demands and confined Li resource have post an apparent conflict. More importantly, by virtue of the dendrite formation of Li anode, the safety hazard turns into enormous challenge, hindering their further applications. It is thus highly essential to investigate earth-abundant and secure alternatives.

It is worth mentioning that above electrolyte with the traits of low cost and high coulombic efficiency has been maturely applied in hybrid systems.^[4–9] Nevertheless, for the sake of avoiding serious corrosion problems, appropriate cathodes with stable electrochemical window (≤ 2.1 V vs Mg/Mg^{2+}) and outstanding electrochemical performances also need to be further investigated.

For cathode materials in Mg-based batteries, almost each types has been widely reported including intercalation compounds,^[9–15] conversion materials,^[16–21] element redox chemistries,^[22–28] water cointercalation materials,^[29–31] as well as hybrid systems.^[4–6,32–35] Among them, intercalation cathodes with unbroken structure during discharge/charge progresses present good cycling stability and become a hot spot in Mg-based batteries, such as chevrel phase,^[4,10] MoS_2 ,^[6,9] spinel Mn_2O_4 ,^[11] TiO_2 ,^[12–14] TiS_2 ,^[15] Ti_2S_4 ,^[36] VS_2 ,^[7] VS_4 ,^[37–39] V_2O_5 ,^[29,40,41] polyanion,^[42] etc. Whereas, they are seriously impeded by low theoretical specific capacity, and more efforts on seeking other high capacity conversion cathodes are still crucial issues.

In recent years, copper-based sulfides with relatively high theoretical capacity (560 mAh g^{-1} for CuS) and high electronic conductivity (103 S cm^{-1}) have emerged as an attractive displacement reaction material toward Mg or hybrid Mg-based batteries. Nevertheless, the main handicap is the intrinsic weakness of the conversion material, that is, the crystal structure

G. Zhu, G. Xia, X. Yu
Department of Materials Science
Fudan University
Shanghai 200438, China
E-mail: yuxuebin@fudan.edu.cn

 The ORCID identification number(s) for the author(s) of this article can be found under <https://doi.org/10.1002/smll.202101845>.

DOI: 10.1002/smll.202101845

will change during the charging and discharging process along with the formation of new phases, which leads to low reversible capacity and poor cycling performance.^[43] In 2016, Nazar et al. first reported CuS microparticles with a size of 5–10 μm in APC electrolyte for RBMs, which shows almost no capacity at room temperature and just delivers a maximum specific capacity of about 60 mAh g⁻¹ and maintains several cycles at an elevating temperature of 60 °C.

Thereafter, considerable effort is focused on rising reversible capacity and cycle stability at low temperature by means of finishing size, increasing interlayer spacing, integrating carbon species,^[44,45] regulating morphologic structure,^[18] introducing hyperbranched polymer^[46] and so on. In terms of the size of materials, cathodes with the features of microspheres,^[20,47] nanoparticles,^[48] hierarchical nanosheets,^[16] ultrafine nanocrystals (20 nm)^[49] were detailedly explored and great progress has been achieved, attaining a reversible capacity of 300 mAh g⁻¹ at 100 mA g⁻¹ for cell assembled by ultrafine CuS nanocrystals cathode. Besides, Shen et al. also demonstrated that interlayer expansion plays an extremely effective factor to enhance the Mg-ion storage and long cycling stability.^[17] Another very crucial method, extensively applied in such materials, is to fabricate porous or hollow structures to improve the utilization rate of active materials and remit the volume expansion. For instance, hollow CuS nanocube with a thin wall is favorable for Mg²⁺ diffusion, and thus realizes a stable capacity of 200 mAh g⁻¹ at 100 mA g⁻¹ and outstanding cycling stability.^[50] In addition, Wang et al. reported that carbon-encapsulated cuprous sulfide (Cu₂S@C) composite is an apparent porous microstructure, delivering an initial specific capacity of 399.2 mAh g⁻¹ at 16.84 mA g⁻¹ and maintaining at ≈150 mAh g⁻¹ after 50 cycles.^[44] However, these previous studies have demonstrated that all of above electrodes are composed in a traditional method, which is the use of insulating and inactive polymer binders and carbon black would inevitably expedite the deterioration of durability and irreversible capacity losses.^[51–54]

It has been demonstrated that the design of binder-free electrodes can effectively solve the deterioration of durability and irreversible capacity losses of electrodes. Naturally, the strategy of fabricating porous nanomaterials through utilizing the volume change of metal–organic frameworks (MOFs) in high molecular weight has an infinite promise, where the porous structure could effectively alleviate the large volume alteration during electrochemical reaction, prevent the structural collapse, and be more facile diffusion of the electrolyte. Therefore, it is highly anticipated that binder-free copper-based sulfides nanoarray with a porous configuration in situ derivation from Cu-MOF precursor could be a promising cathode material for Mg-based batteries, which, however, has received few attention so far. In this work, we demonstrate a strategy to synthesize Cu-MOF template-derived hierarchical cuprous sulfide porous nanosheet decorated nanowire arrays self-assembled on copper foam (Cu₂S HP/CF). The as-synthesized foils could be directly employed as cathode for MLIB without additional conductive additives or binders and other coating processes, implementing a high reversible specific capacity of 311 mAh g⁻¹ at 100 mA g⁻¹ at room temperature and excellent cycle life (129 mAh g⁻¹ at 300 mA g⁻¹ over 500 cycles).

2. Results and Discussion

Hierarchical Cu₂S porous nanostructure was generated by the volume change of MOFs in high molecular weight. The stepwise synthesis of Cu₂S/CF, Cu₂S NW/CF, and Cu₂S HP/CF is depicted in **Figure 1a**. At the outset, the fresh CF is yellow and smooth. After being engraved in alkaline solution, a large number of green Cu(OH)₂ nanowires in situ generate uniformly on the CF substrate. Whereafter, Cu-MOF on CF (Cu-MOF/CF) with a relatively thick and cross-linked feature is successfully gained via applying Cu(OH)₂ NW/CF as precursor, terephthalic acid (PTA) as ligands and *N,N*-dimethylformamide (DMF) as solvent. In the end, corresponding sulfides are obtained through a simple low-temperature sulfidation process under the same condition. Interestingly, as the Cu(OH)₂ precursor is prepared by in situ formation of engraving CF, the CF can directly employed as current collector with the merits of avoiding the use of polymeric binder. Such electrode is of great benefit for facilitating the structural stability and providing high Mg²⁺/Li⁺ flux and consecutive and fast conductive paths throughout electrode, which would greatly improve the cycle performance and electrochemical property.

Figure 1b and Figure S1a (Supporting Information) depict the scanning electron microscopy (SEM) images of bare CF, presenting a smooth surface. After undergoing a simple engraving process in alkaline solution, the surface of CF is fully covered with Cu(OH)₂ nanowires (Figure 1c; Figure S1b, Supporting Information). As shown in the magnified SEM image (inset of Figure 1c), the Cu(OH)₂ nanowire presents a smooth surface with a large diameter of ≈200 nm. Interestingly, after a solvothermal growth with DMF solution and PTA ligand, the resulting Cu-MOF completely transform into thick, interconnected and irregular nanosheets with the disappearance of nanowire characteristics (Figure 1d; Figure S1c, Supporting Information). Notably, the vanishment of nanowires structure also signifies that the Cu(OH)₂ has been totally turned into Cu-MOF. First, we prepared Cu₂S/CF by directly using bare CF as precursor. As illustrated in Figure 1e and Figure S1d (Supporting Information), the morphology is in accord with bare CF and emerges the shape of the Cu₂S grain on smooth surface, indicating an extremely finite specific area and few expansion space. Second, Cu(OH)₂ NW/CF was also utilized as a precursor, vulcanized under the same condition. Due to a small volume change, the as-prepared Cu₂S NW/CF still maintains a solid nanowire feature with a similar diameter but shows a rough surface, which is consistent with the Cu₂S/CF (Figure 1f; Figure S1e, Supporting Information). Compared with Cu₂S/CF, such nanoarchitecture has a larger specific surface area and more room for lateral expansion. It is worth noting that Cu₂S HP/CF, which was synthesized via employing Cu-MOF in relatively high molecular weight as precursor presents a hierarchical nanoarray architecture (Figure 1g–i; Figure S1f, Supporting Information). High magnification image obviously manifests that such hierarchical structure with multiple directions of secondary porous nanosheets on the primary nanowires, where porous structure can be ascribed to the volume change resulting from the removal of organics from the Cu-MOF during sulfuration. Moreover, the interconnections between the extended porous nanosheets and these secondary

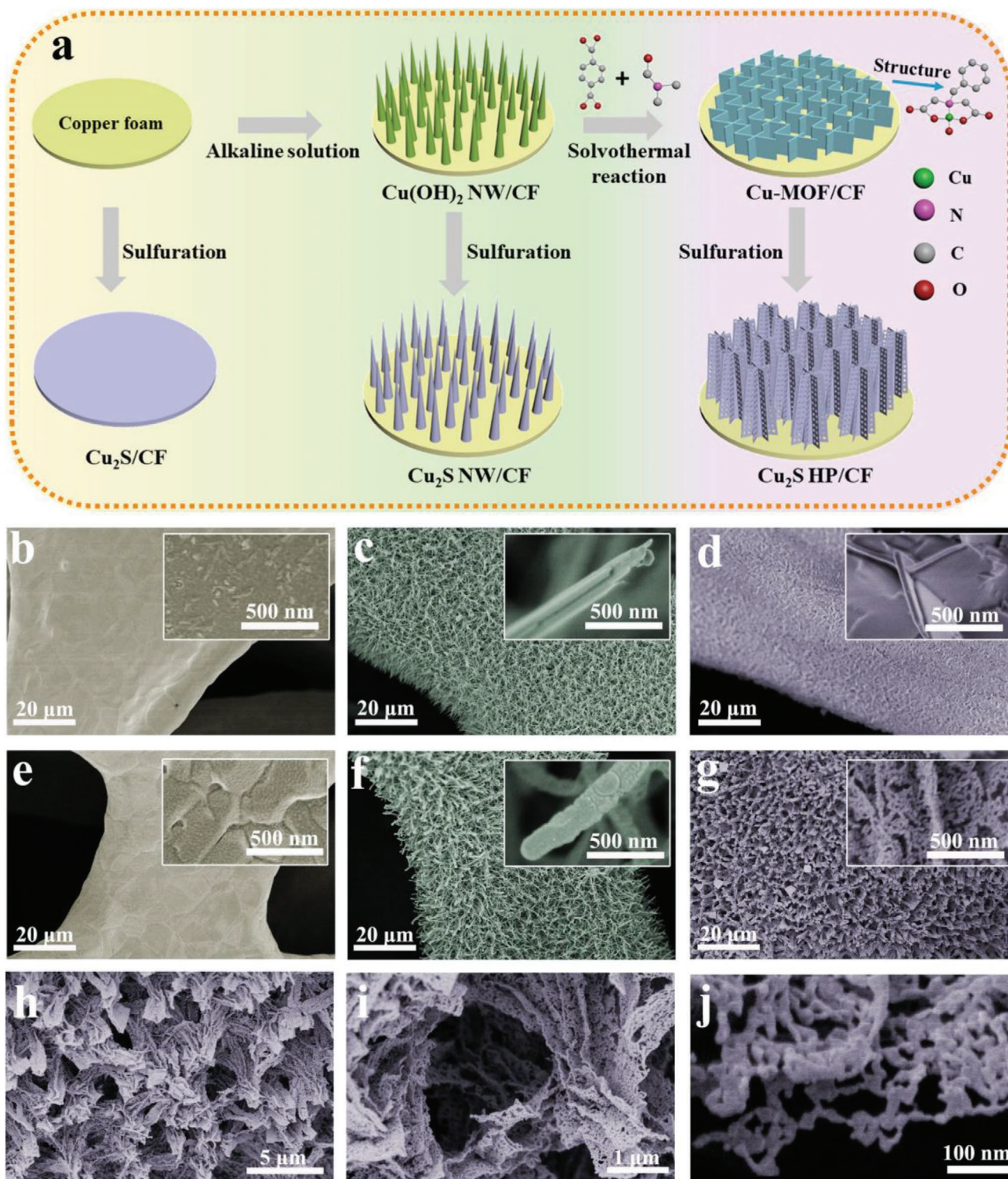


Figure 1. a) Schematic illustration of the fabrication for $\text{Cu}_2\text{S}/\text{CF}$, $\text{Cu}_2\text{S NW}/\text{CF}$, and $\text{Cu}_2\text{S HP}/\text{CF}$. SEM images of b) bare CF, c) $\text{Cu}(\text{OH})_2 \text{ NW}/\text{CF}$, d) $\text{Cu-MOF}/\text{CF}$, e) $\text{Cu}_2\text{S}/\text{CF}$, f) $\text{Cu}_2\text{S NW}/\text{CF}$, and g–j) $\text{Cu}_2\text{S HP}/\text{CF}$.

structures connect adjacent nanowires and such morphology is integrated to align vertically on CF. Figure S2 of the Supporting Information shows the SEM image and the corresponding energy-dispersive X-ray spectroscopy (EDX) elemental

mapping images, verifying the uniform distribution of Cu and S elements throughout the $\text{Cu}_2\text{S HP}/\text{CF}$. Furthermore, the EDX analysis demonstrates that the molar ratio of Cu and S is 42.8:20.3, which is close to the theoretical value, and the excess

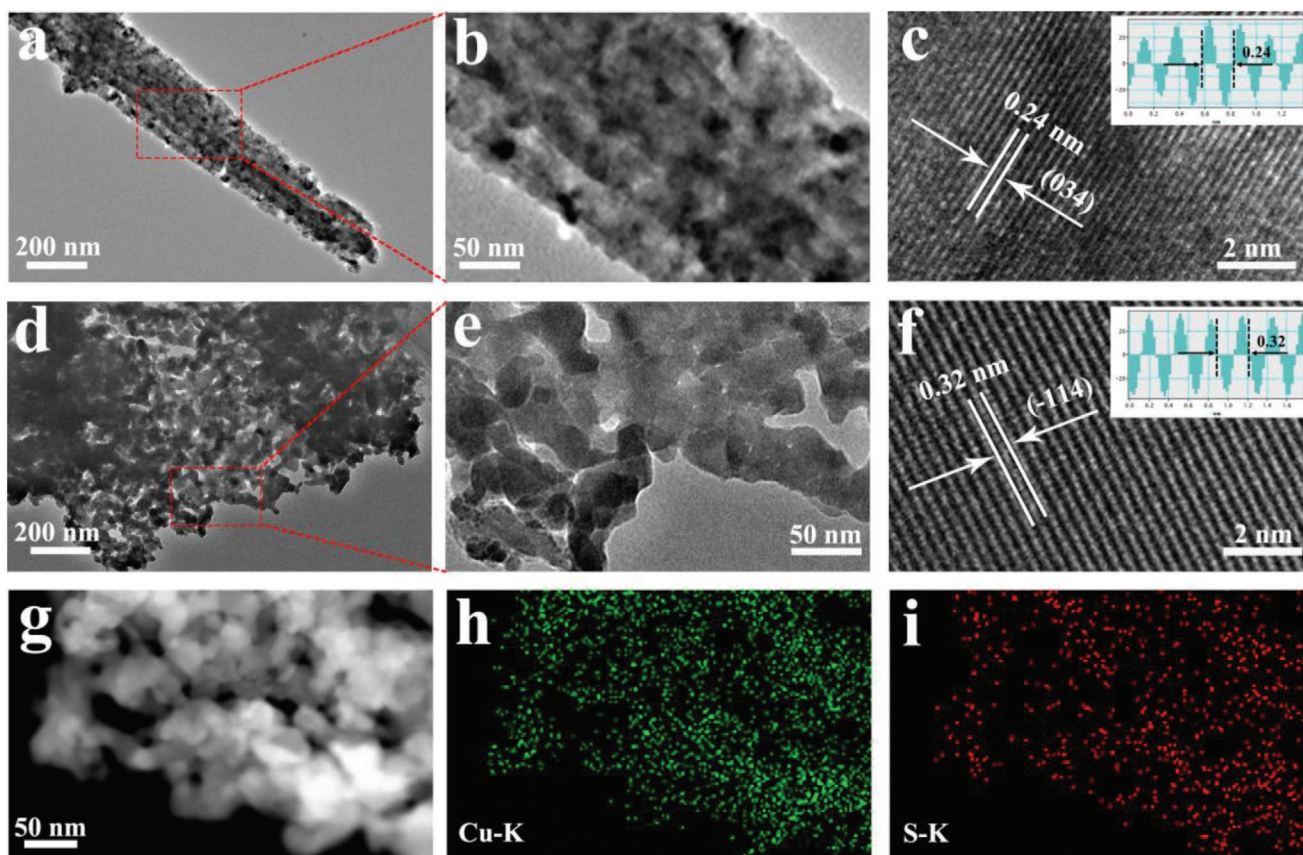


Figure 2. a,b) TEM images and c) HRTEM image of Cu₂S NW. d,e) TEM images and f) HRTEM image of Cu₂S HP. g) The scanning transmission electron microscopy (STEM) image and h,i) the elemental maps of Cu₂S HP (Cu and S).

of Cu is due to the exposure of CF. Notably, corresponding powder sample still maintains analogous nanoporous feature but without the hierarchical structure (Figure S3, Supporting Information).

The morphology of the as-synthesized Cu₂S NW/CF and Cu₂S HP/CF was further characterized by transmission electron microscopy (TEM). **Figure 2a,b** shows the low-magnification TEM images of one single Cu₂S nanowire, confirming a solid nanowire feature with a large diameter of about 200 nm. The corresponding high-resolution TEM (HRTEM) image in **Figure 2c** clearly exhibits lattice fringe of 0.24 nm, which is well indexed to the (034) plane of Cu₂S phase. **Figure 2d,e** displays the TEM images of a slice of an incomplete nanosheet exfoliated from Cu₂S HP/CF, further suggesting the existence of porous feature and corresponding to the SEM results. Such porous morphology is beneficial for boosting specific capacity and cycling life through increasing the contact surface between electrolyte and material, reducing electron transport distance, and providing sufficient expansion space. Besides, HRTEM analysis (**Figure 2f**) is in accord with the interplanar spacing of 0.32 nm and agrees well with (-114) plane of Cu₂S phase. Additionally, **Figure 2g-i** presents the scanning transmission electron microscopy (STEM) image and the elemental mapping images of Cu and S, offering more evidence for the uniform distribution of a single porous sheet.

Figure 3a and **Figure S4** (Supporting Information) demonstrate the X-ray diffraction (XRD) patterns of Cu₂S HP/CF, Cu(OH)₂ NW/CF, and Cu-MOF/CF, where three strong diffraction peaks at 43.3°, 50.5°, and 74.2° can be indexed to CF substrate. The sample that engraves CF in alkaline solution is well matched to Cu(OH)₂ phase (JCPDS No. 13-0420), in which the reaction can be expressed as $\text{Cu} + 4\text{NaOH} + (\text{NH}_4)_2\text{S}_2\text{O}_8 \rightarrow \text{Cu}(\text{OH})_2 + 2\text{Na}_2\text{SO}_4 + 2\text{NH}_3\uparrow + 2\text{H}_2\text{O}$.^[54] Following a solvothermal reaction, the product displays characteristic peaks of C₁₁H₁₁CuNO₅ (CCDC No. 687690) without the signal of Cu(OH)₂, which is in keeping with the disappearance of nanowire structure in the SEM images of Cu-MOF/CF. Notably, the formation of Cu-MOF can be illustrated as $\text{Cu}(\text{OH})_2 + \text{C}_6\text{H}_4(\text{COOH})_2 + \text{C}_3\text{H}_7\text{ON} (\text{DMF}) \rightarrow \text{C}_{11}\text{H}_{11}\text{CuNO}_5 (\text{Cu-MOF}) + 2\text{H}_2\text{O}$.^[55] After sulfidizing at low temperature in Ar atmosphere, the diffraction peaks of the as-prepared sulfide product can be assigned to pure Cu₂S phase (JCPDS No. 33-0490), indicating the formation of Cu₂S HP/CF. For comparison, bare CF and Cu(OH)₂ NW/CF employed as precursor were performed identical sulfuration progress under the same condition. As depicted in **Figure S5** of the Supporting Information, all peaks are consistent with Cu₂S phase (JCPDS No. 33-0490), manifesting the successful synthesis of Cu₂S/CF and Cu₂S NW/CF. Fourier transform infrared (FTIR) measurement is carried out to further analyze the structure of Cu-MOF (**Figure 3b**). Specifically, the strong peaks at 1628 and 1393 cm⁻¹ are ascribed to

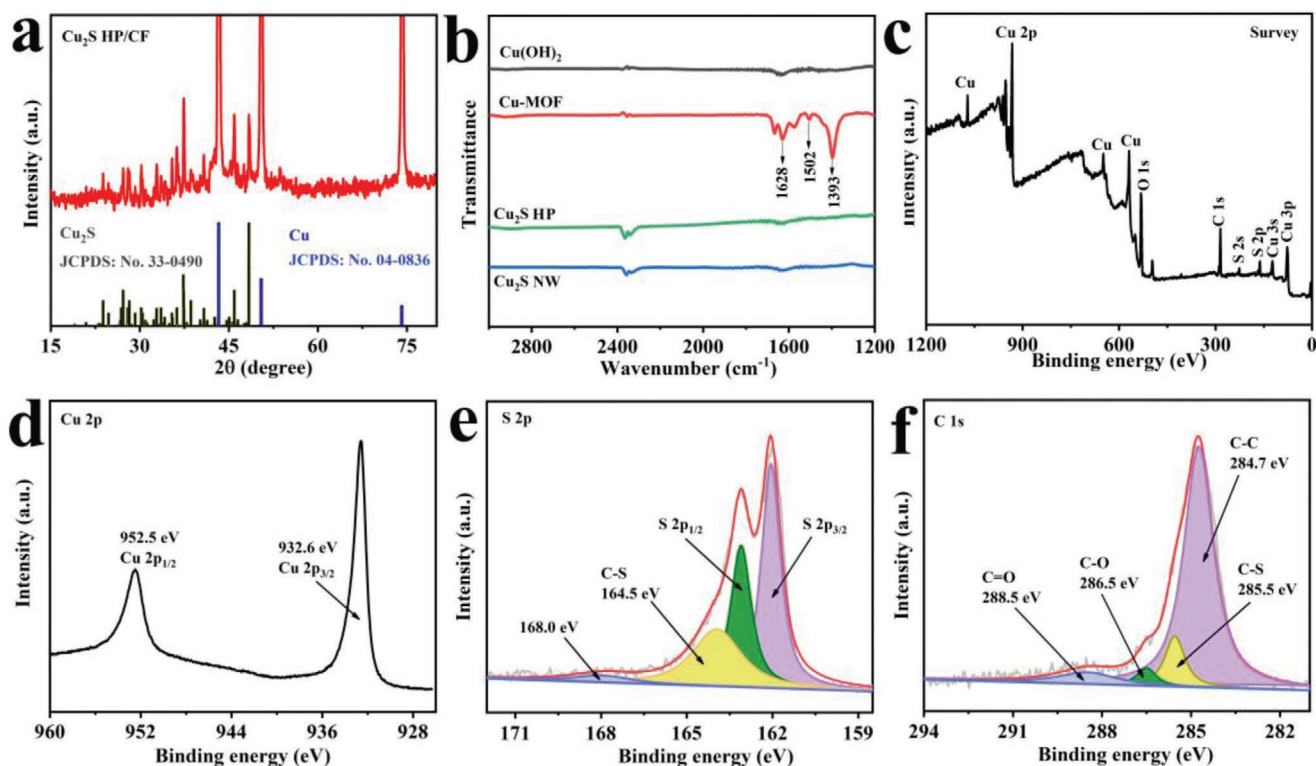


Figure 3. a) XRD patterns of Cu_2S HP/CF. b) FT-IR spectra of $\text{Cu}(\text{OH})_2$, Cu-MOF, Cu_2S HP, and Cu_2S NW. c) XPS survey spectrum, for Cu_2S HP/CF. XPS spectra for Cu_2S HP/CF in the d) Cu 2p, e) S 2p, and f) C 1s regions.

the asymmetric and symmetric stretching modes of the coordinated ($-\text{COO}$) group, respectively, and the peak at 1502 cm^{-1} can be assigned to the para-aromatic C–H groups.^[55] It is worth mentioning that the sulfide sample has no corresponding characteristic peaks, suggesting that Cu-MOF is completely converted into Cu_2S phase. In addition, thermogravimetric analysis (TGA) is conducted to obtain the percentage of carbon. As shown in Figure S6 of the Supporting Information, there is a low loading ratio (about 5.6 wt%) of carbon in Cu_2S HP/CF, while Cu_2S NW/CF has few weight loss under air atmosphere from ambient temperature to $800\text{ }^\circ\text{C}$. Importantly, the existence of a small amount of carbon in the Cu_2S HP/CF can facilitate the conductivity of active material. Considering that the Cu_2S HP/CF contains CF substrate and the powder sample has a very analogous morphology, Cu_2S HP powder was employed to assess the specific surface area and pore size distribution of the Cu_2S HP/CF. According to the N_2 adsorption/desorption measurement (Figure S7, Supporting Information), the Brunauer–Emmett–Teller (BET) specific surface area is $\approx 19.7819\text{ m}^2\text{ g}^{-1}$ and the pore sizes are mainly distributed in 2.5–13.44 nm. It should be noted that the practical specific surface area of Cu_2S in Cu_2S HP/CF should have a higher value, since the binder-free product has a merit of 3D hierarchical feature.

To further verify the chemical composition and valence states of Cu_2S HP/CF, X-ray photoelectron spectroscopy (XPS) measurement was also recorded. The XPS survey spectrum (Figure 3c) confirms the presence of Cu, S, C, and O elements in Cu_2S HP/CF. Figure 3d–f displays the high-resolution XPS spectra of Cu 2p, S 2p, and C 1s. In the Cu 2p spectrum

(Figure 3c), two peaks at 952.5 and 932.6 eV are attributed to the binding energies (BEs) of Cu $2p_{1/2}$ and Cu $2p_{3/2}$, respectively, corresponding to the core level of Cu^+ .^[44] Figure 3d depicts the fitted spectrum of S 2p, in which the two main peaks with the BEs at 162.1 and 163.1 eV can be assigned to S $2p_{1/2}$ and S $2p_{3/2}$, respectively.^[56] Besides, the broadened peak which appears at 164.5 eV can be ascribed to C–S bond in the composite, while an extra peak at 168.0 eV is due to the formation of Cu_2S . The C 1s core-level spectrum in Figure 3f demonstrates peaks at 288.5, 286.5, 285.5, and 284.7 eV, corresponding to the BEs of C=O, C–O, C–S, and C–C bonds, respectively.^[57] All these results confirm that the as-prepared sulfide product is Cu_2S .

Figure 4 exhibits the electrochemical performance of $\text{Cu}_2\text{S}/\text{CF}$, Cu_2S NW/CF, Cu_2S HP/CF, and scraped Cu_2S HP powder cathodes. The cyclic voltammetry (CV) data of three binder-free electrodes were measured at a scan rate of 0.1 mV s^{-1} with a voltage range of 0.1–1.85 V. The CV curves of as-obtained cathodes shown in Figure 4a display the same redox stages with main peak voltages at 1.65 and 1.06 V, respectively. Compared with $\text{Cu}_2\text{S}/\text{CF}$ and Cu_2S NW/CF, the Cu_2S HP/CF shows obviously sharp reduction peak at 1.06 V, which could ascribe to an increased conversion reaction of Mg and Li. Obviously, this phenomenon is well verified by corresponding charge and discharge curves at a current density of 100 mA g^{-1} (Figure 4b), where the discharge plateau centered at about 1.06 V in Cu_2S HP/CF electrode is extraordinarily evident, indicating a very complete conversion reaction and contributing most of specific capacity. Such case can be explained by the unique hierarchical porous structure that is favorable for enhancing contact surface

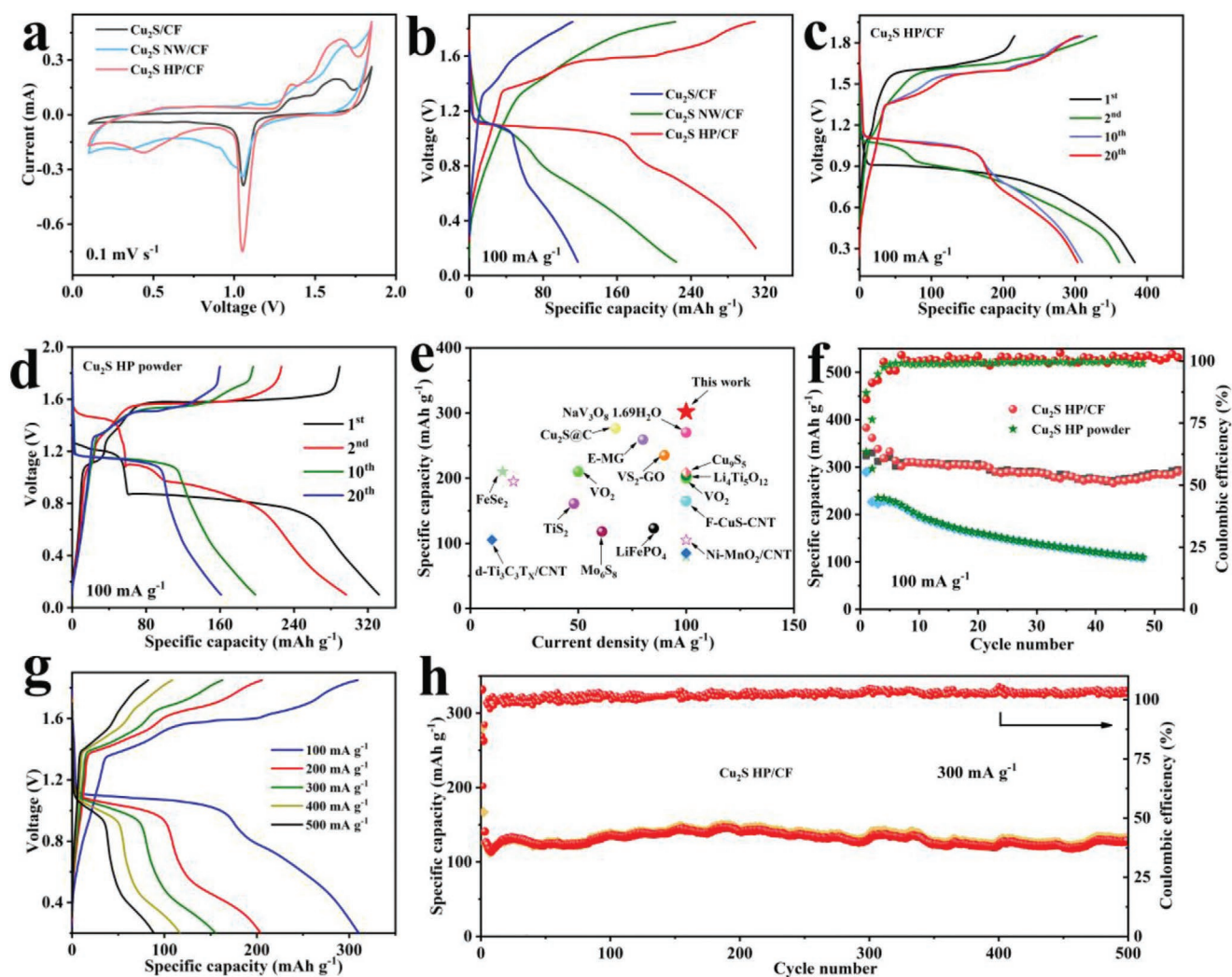


Figure 4. a) CV curves and b) galvanostatic charge–discharge voltage profiles of $\text{Cu}_2\text{S}/\text{CF}$, $\text{Cu}_2\text{S NW}/\text{CF}$, and $\text{Cu}_2\text{S HP}/\text{CF}$. Galvanostatic charge–discharge voltage profiles of c) $\text{Cu}_2\text{S HP}/\text{CF}$ and d) $\text{Cu}_2\text{S HP}$ powder cathodes at a current density of 100 mA g^{-1} . e) Comparison of reversible capacity of the state-of-the-art cathodes for various reported $\text{Mg}^{2+}/\text{Li}^+$ hybrid battery systems. Cycling performance and coulombic efficiencies at current densities of f) 100 mA g^{-1} and h) 300 mA g^{-1} . g) Galvanostatic charge and discharge profiles of the $\text{Cu}_2\text{S HP}/\text{CF}$.

between electrolyte and Cu_2S and reducing electron transport distance to ensure the reaction taking place adequately. Figure 4c and Figure S8a,b (Supporting Information) reveal the galvanostatic charge/discharge profiles of $\text{Cu}_2\text{S}/\text{CF}$, $\text{Cu}_2\text{S NW}/\text{CF}$, and $\text{Cu}_2\text{S HP}/\text{CF}$ at 100 mA g^{-1} between 0.1 and 1.85 V over different cycles. The voltage plateaus entered at about 1.06 V in discharge curve and 1.65 V in charge profile are in conformity with the cathodic and anodic peaks in CV curves. The initial discharge capacity of 383 mAh g^{-1} is afforded over $\text{Cu}_2\text{S HP}/\text{CF}$ cathode, which is much higher than that of $\text{Cu}_2\text{S}/\text{CF}$ and $\text{Cu}_2\text{S NW}/\text{CF}$ cathodes (170 and 330 mAh g^{-1} , respectively). In the subsequent cycles, the voltage curves clearly show that the voltage plateaus are well maintained, manifesting an outstanding reversibility during cycling. The reversible capacity for $\text{Cu}_2\text{S HP}/\text{CF}$ can implement 311 mAh g^{-1} at 10th cycle that is larger than that for $\text{Cu}_2\text{S}/\text{CF}$ and $\text{Cu}_2\text{S NW}/\text{CF}$ (117 and 252 mAh g^{-1} , respectively). More significantly, the cathode obtained in a traditional strategy was also brought in to affirm

the preponderance of binder-free electrode. As shown in Figure 4d, the powder electrode also exhibits an obvious discharge voltage plateau and delivers a high initial discharge capacity of 332 mAh g^{-1} , but just has a low specific capacity of 161 mAh g^{-1} after 20 cycles. The markedly enhanced specific capacities and cycle life of $\text{Cu}_2\text{S HP}/\text{CF}$ can be attributed to the unique array feature and to the fact that the in situ generated cathode has binder-free trait. Notably, the performance of $\text{Cu}_2\text{S HP}/\text{CF}$ outperforms most reported intercalation cathodes ($\text{d-Ti}_3\text{C}_3\text{T}_x/\text{CNT}$, TiS_2 , Mo_6S_8 , VO_2 , E-MG, $\text{VS}_2\text{-GO}$, $\text{NaV}_3\text{O}_8 \cdot 1.69\text{H}_2\text{O}$, etc.) and most studied conversion materials ($\text{Cu}_2\text{S}@C$, Cu_9S_5 , F-CuS-CNT, etc.) in hybrid MLIBs (Figure 4e; Table S3, Supporting Information). Furthermore, several conversion type cathode materials for MIBs, such as Cu-based chalcogenides, have also been summarized in Table S4 of the Supporting Information.

Considering that the structure can be well remained during discharge/charge process for intercalation cathodes, such

categories of materials are outstanding for its excellent cycle life and fast ion diffusion. Unfortunately, the low theoretical capacity posts an irreparable flaw in their application as a perfect cathode. Conversion materials with the superiority of obviously high theoretical capacity have also received much concern. Even more important, as the cycling stability is the overriding consideration for such kinds of materials, we paid more attention on investigating the cycling performance of as-synthesized cathodes. Figure S6c shows the cycling curves and coulombic efficiency (CE) of $\text{Cu}_2\text{S}/\text{CF}$ and $\text{Cu}_2\text{S NW}/\text{CF}$. As expected, the $\text{Cu}_2\text{S}/\text{CF}$ delivers a very small reversible capacity of 118 mAh g^{-1} at 100 mA g^{-1} at 10th cycle, and decreases to 62 mAh g^{-1} after undergoing 50 cycles. There is no doubt that the reason for poor capacity retention rate belongs to the absence of available expansion space, which dramatically hampers the full utilization of active sites. By contrast, the $\text{Cu}_2\text{S NW}/\text{CF}$ with more accessible surface and numerous expansion area along the diameter of nanowire structure realizes significantly improved specific capacity, with the accomplishment of 252 and 169 mAh g^{-1} at 100 mA g^{-1} over 10 and 50 cycles, respectively. Even more significant, Figure 4f displays that $\text{Cu}_2\text{S HP}/\text{CF}$ exhibits superior capacity retention over that for $\text{Cu}_2\text{S}/\text{CF}$ and $\text{Cu}_2\text{S NW}/\text{CF}$, with a high specific capacity of 284 mAh g^{-1} after 50 cycles at the same current density. Compared with $\text{Cu}_2\text{S NW}/\text{CF}$ cathode, the reason for further improvement of cycle life lies not only in the expansion space in the direction of the thickness of nanosheet in hierarchical structure, but also in the more axial area created by the porous feature in such sheet. These extra space can effectively alleviate the pressure strain and promote the contact between electrode and electrolyte during the charge and discharge process. Clearly, due to the utilization of the polymer binder, the powder electrode demonstrated in Figure 4f exhibits lower specific capacity and poorer cycling stability. In addition, the CE for all four cathodes is close 100%, except that the CE of $\text{Cu}_2\text{S}/\text{CF}$ is a little lower in the beginning of 20 cycles (Figure S8c, Supporting Information). For investigating the influence of carbon, we also synthesized carbon-free cathode via annealing Cu-MOF precursor under air atmosphere to remove carbon sources. The morphology of C-free $\text{Cu}_2\text{S HP}$ powder is very similar to $\text{Cu}_2\text{S HP}$ powder (Figure S9, Supporting Information). The electrochemical performance of C-free $\text{Cu}_2\text{S HP}$ powder indicates that the plateau and the cycling performance are analogous to $\text{Cu}_2\text{S HP}$ powder, but the specific capacity is a little bit lower than that of $\text{Cu}_2\text{S HP}$ powder (Figure S10, Supporting Information). Above results manifest that the electrochemical performance of Cu_2S is slightly affected by carbon, where the primary reason may be ascribed to the “nanoarray.”

Furthermore, the rate capability of $\text{Cu}_2\text{S HP}/\text{CF}$ shown in Figure S11 of the Supporting Information delivers reversible discharge capacities of about 315, 215, 149, 102, and 71 mAh g^{-1} at 100, 200, 300, 400, and 500 mA g^{-1} , respectively. Interestingly, when the current density reverts to 100 mA g^{-1} after 30 cycles, a high capacity of 297 mAh g^{-1} can be achieved, suggesting good tolerance and excellent cycling stability. In sharp contrast, $\text{Cu}_2\text{S NW}/\text{CF}$ displays much lower capacities at the same current densities and the $\text{Cu}_2\text{S}/\text{CF}$ gets further small values. The galvanostatic charge and discharge profiles are displayed in Figure 4g, manifesting well maintenance of the shape of the

curve and the plateau. In addition, the shape and the plateau can be well kept for the powder sample, just delivers obviously low capacities (Figure S12, Supporting Information), indicating that the binder-free electrode has more advantages in improving the specific capacity. Even more momentous is the fact that the long-term cycling performance is a pivotal parameter for conversion materials. The MLIBs based on as-fabricated materials were performed at 300 mA g^{-1} (Figure 4h; Figure S13, Supporting Information). The $\text{Cu}_2\text{S HP}/\text{CF}$ shows an outstanding stability with an admirable capacity of 129 mAh g^{-1} after 500 cycles, which is far ahead of the $\text{Cu}_2\text{S NW}/\text{CF}$ (94 mAh g^{-1} after 436 cycles) and $\text{Cu}_2\text{S}/\text{CF}$ (38 mAh g^{-1}). Particularly, the CE unexpectedly rises when the $\text{Cu}_2\text{S NW}/\text{CF}$ undergoes 430 cycles and the cell is broken, indicating its poor durability. Particularly, the SEM and STEM images in Figures S14 and S15 of the Supporting Information reveal that the nanoarray morphology and porous structure is well retained after cycling test. Besides, the elements are evenly distributed, and the signal of Mg is very weak, which can be attributed to the fully charged state.

Electrochemical impedance spectra (EIS) analysis was conducted for the sake of intrinsically probing the ion diffusion kinetics. As depicted in Figure S16 of the Supporting Information, the ohmic resistance of electrolyte and cell is represented by R_s , while R_{ct} is on behalf of the charge-transfer resistance. The $\text{Cu}_2\text{S HP}/\text{CF}$ has a smaller semicircle diameter compared with the $\text{Cu}_2\text{S NW}/\text{CF}$ and $\text{Cu}_2\text{S}/\text{CF}$, uncovering lower charge-transfer resistance ($R_{ct} = 76.86 \Omega$). Additionally, optimized electrode shows a straight line with a higher slope (Warburg impedance, W_o), which elucidates easier ion diffusivity within electrode.

In order to probe the function of Li^+ in hybrid system, electrolytes with different LiCl concentrations were introduced to investigate the performance of $\text{Cu}_2\text{S HP}/\text{CF}$. The voltage profiles and cycling ability are presented in Figure S17 of the Supporting Information, displaying obviously low initial and stable reversible capacities in pure MIBs (0 M LiCl ; 233 and 75 mAh g^{-1} , respectively) and very small discharge plateau. The reasons of poor Mg^{2+} storage performance of Cu_2S nanoarrays are mainly resulted from the employed electrolyte (APC/tetrahydrofuran (THF)) in this study. Previous reports have demonstrated that copper sulfide cathode with APC/THF electrolyte at room temperature presents low capacities compared to other electrolyte (achieving about 80 mAh g^{-1} at 20 mA g^{-1} after 12 cycles for CuS and about 35 mAh g^{-1} at 16.84 mA g^{-1} after 45 cycles for Cu_2S).^[20,44] When the LiCl is added (from 0.4 to 1.0 M), the discharge plateau is becoming more and more obvious, and the discharge capacities also gradually increased. The inductively coupled plasma mass spectrometry (ICP-MS; Table S1, Supporting Information), element mappings and EDX spectra (Figure S18 and Table S2, Supporting Information) results in MIBs and MLIBs (1.0 M LiCl) after discharged to 0.1 V demonstrate that the ratios of Mg:Cu and (Mg-2Cl):Cu in MLIBs are more than that in MIBs, revealing an enhanced conversion of Mg^{2+} in MLIBs. Intriguingly, the cycling stability is outstanding under every electrolyte. Therefore, the main role of lithium salt in electrolyte is to greatly boost the utilization of materials via facilitating the insertion/extraction of Mg^{2+} and introducing the conversion of Li, but few influence on the lifespan. The EIS plots of $\text{Cu}_2\text{S HP}/\text{CF}$ in MIBs and MLIBs demonstrate that the

addition of lithium salt reduces the charge transfer impedance and accelerates the ion diffusion within electrode (Figure S19, Supporting Information).

To further scrutinize the effect of lithium additives and evaluate the function of the constructed hierarchical structure and binder-free feature, galvanostatic intermittent titration diffusion technique (GITT) was employed to analyze the Mg^{2+} and $\text{Li}^+/\text{Mg}^{2+}$ solid-state diffusion in Cu_2S HP powder and Cu_2S HP/CF cathodes in the first cycle (Figure S20, Supporting Information). The GITT method was conducted by applying a constant current flux of 10 mA g^{-1} for a limited time period. Whereafter, the diffusion coefficient of Mg^{2+} and $\text{Li}^+/\text{Mg}^{2+}$ is calculated by the following formula^[58]

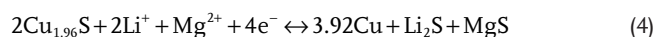
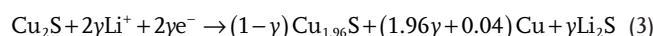
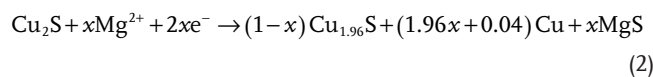
$$D^{\text{GITT}} = \frac{4}{\pi\tau} \left(\frac{m_B V_M}{M_B S} \right)^2 \left(\frac{\Delta E_s}{\Delta E_t} \right)^2 \quad (1)$$

where τ , m_B , V_M , M_B , and S correspond to the constant current pulse time, mass, molar volume, molar mass, and electrode–electrolyte interface area of two cathodes, respectively. ΔE_s and ΔE_t are the voltage change during the open-circuit period and a constant current pulse period, respectively. In the comparison between powder product and binder-free sample (Figure S20d, Supporting Information), the average diffusion coefficient of Cu_2S HP/CF is higher in MIBs, indicating faster Mg^{2+} transfer kinetics in constructed multistage structure and binder-free material. Figure S20e of the Supporting Information reveals that the average diffusion coefficient of Mg^{2+} is obviously lower than that of $\text{Li}^+/\text{Mg}^{2+}$ in binder-free sample. From what is gained above, a conclusion that the addition of lithium salt can effectively enhance ions migration rate can be drew.

To accurately assess the electrochemical kinetics of Cu_2S HP/CF cathode, CV testing at various scan rates from 0.1 to 0.8 mV s^{-1} was also carried out. The CV profiles in Figure S21 of the Supporting Information show similar shapes at different scans, but redox currents (i) present a linear increasing trend as the increase of scan rate (v). Additionally, there is a slightly increased electrochemical polarization, which can be faultlessly expounded by the enhanced voltage gap in redox peaks. It is well known that the relationship between i and v can be summed up to $i = av^b$, in which a and b are the adjustable parameters. According to previously reported studies, b value fitted by the relationship between $\log i$ and $\log v$ plots can be conducted to estimate the electrochemical rate-determining processes, where diffusion-controlled reaction and capacitive behavior will hinge on b values of 0.5 and 1.0, respectively. Herein, that values of discharge/charge stages were calculated to be 0.56 and 0.57, illustrating that both discharge and charge reaction processes are dominated by diffusive behavior. Beyond that, EIS analysis in Figure S22 of the Supporting Information is performed to demonstrate the electrode kinetics of Cu_2S HP/CF at various states. The test results display that with the increase of cycles, the diameter of the semicircle decreases and the slope of the line increases, indicating the reduced charge-transfer impedance and easier ion diffusivity.

In order to research the electrochemical reaction mechanism, ex situ XRD, XPS, and TEM measurements were performed at

various stages. Figure 5a,b shows the ex situ XRD results of Cu_2S HP/CF with APC + LiCl hybrid electrolyte during the first cycle. The strongest characteristic peaks located on 43.3° and 50.4° in every state are assigned to CF. In the first place, pristine Cu_2S HP material coordinates well with the peaks of Cu_2S phase. When discharged to 1.1 V (b site in Figure 5b) at 50 mA g^{-1} , with the disappearance of original peaks, new characteristic peaks appear at 32.7° , 39° , and 45.4° , corresponding to (103), (104), and (200) crystal face of $\text{Cu}_{1.96}\text{S}$ (JCPDS No. 29-0578) with space group of $P43212$ (96). After the following discharge to 0.9 V (c site), the signal of $\text{Cu}_{1.96}\text{S}$ is still obvious but accompanied by the weak peak of MgS phase, implying incomplete conversion from $\text{Cu}_{1.96}\text{S}$ to metal Cu and MgS. Upon further discharge to 0.2 V (d site), the cathode presents no other reflections except for two peaks of MgS (JCPDS No. 35-0730) phase in the XRD pattern, while another peak of MgS is not obvious, since it is close to Cu. The reason why there are no other peaks is that the overlap of metal Cu and CF. It is worth noting that the peaks of MgS almost vanish with resurfacing $\text{Cu}_{1.96}\text{S}$ phase after fully charging to 1.85 V (d site). Because XRD test does not detect the signal of Li_2S , we also explore XPS analysis to confirm the involvement of Li^+ and the reversible conversion reaction of Mg^{2+} . As depicted in Figure 5c, no signal of Li is detected in the original Cu_2S HP/CF, but that signal appears when discharged to 0.1 V and the peak nearly vanishes after charging to 1.85 V. The Mg 1s XPS pattern in Figure 5d demonstrates similar phenomenon but has a weak signal when charged to 1.85 V. For making sure the formation of Cu and Li_2S after discharging to 0.1 V and further determining the reaction mechanism of Mg^{2+} and Li^+ storage, HRTEM and selected area electron diffraction (SAED) measurements of Cu_2S HP/CF at the fully discharged state were introduced (Figure 5e–h). Both HRTEM and SAED verify the successful generation of Cu and Li_2S , suggesting that the fully discharged material is made up of MgS, Li_2S , and metallic Cu. On the basis of above analyses, the Mg^{2+} and Li^+ storage mechanism of Cu_2S electrode can be expressed to be a two-step conversion reaction (Equations (2)–(4)), in which Equations (2) and (3) are reacting at the same time and are irreversible process (Figure 5i)



3. Conclusion

In summary, a facile strategy was developed to fabricate self-assembled Cu_2S with hierarchical nanoporous cluster arrays feature that is homogeneously grown in situ on CF. Abundant porous morphology is successfully implemented via making full use of the volume change of MOF material during sulfuration process. Such a 3D material was employed as a novel binder-free cathode for hybrid $\text{Mg}^{2+}/\text{Li}^+$ battery, accomplishing an impressively reversible specific capacity of 311 mAh g^{-1} at 100 mA g^{-1} with outstanding cycling performance. Hierarchical

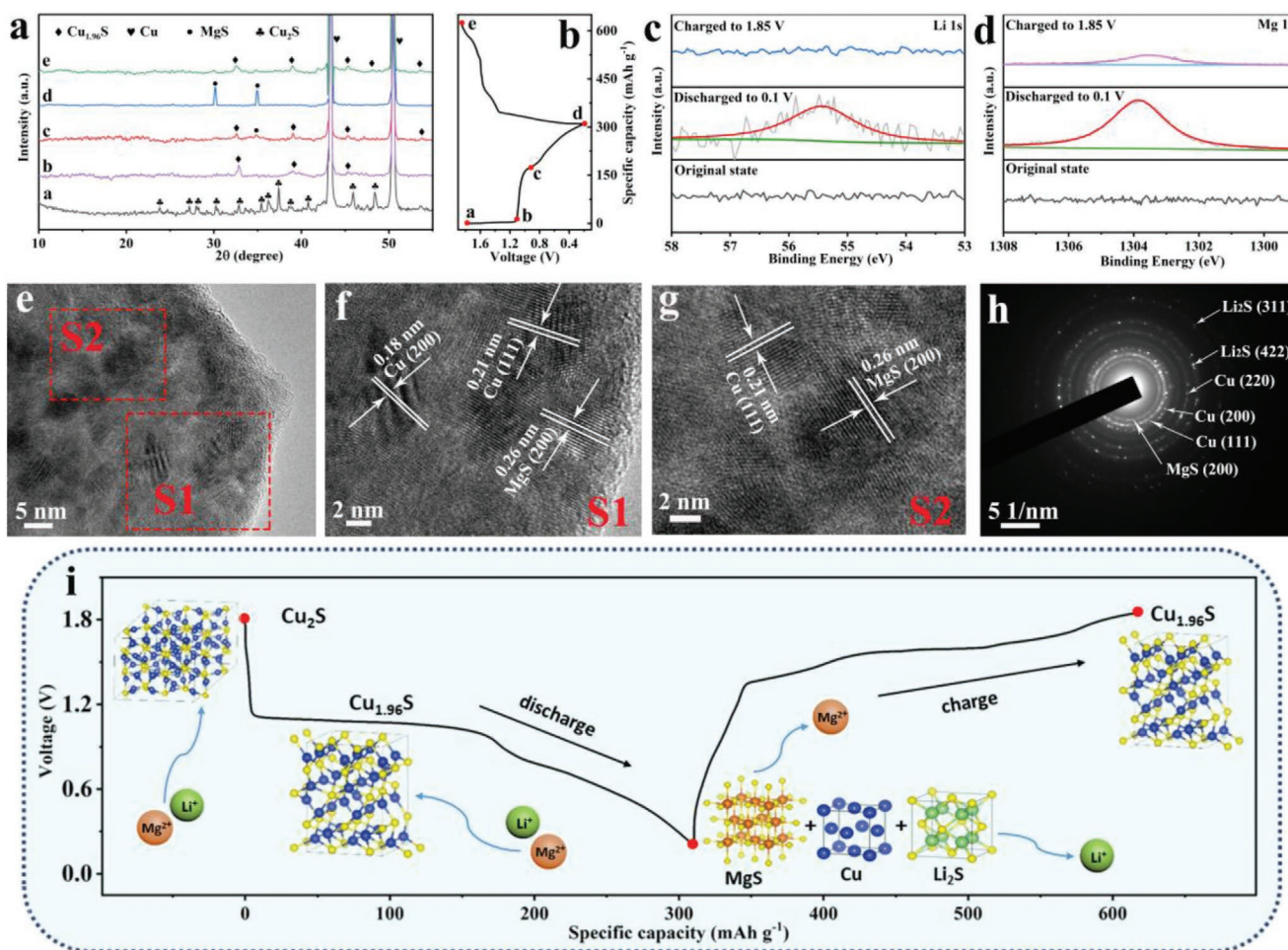


Figure 5. a) Ex situ XRD patterns of the Cu₂S HP/CF electrode at different electrochemical states: a: as-prepared; b: first discharge to 1.1 V; c: first discharge to 0.9 V; d: first discharge to 0.1 V; e: first charge to 1.85 V. b) Galvanostatic charge and discharge curve of the Cu₂S HP/CF cathode at 50 mA g⁻¹. c) High-resolution XPS spectra of Cu₂S HP/CF before and after cycling: c) Li 1s and d) Mg 1s. e–g) HRTEM images and h) SAED pattern of Cu₂S HP/CF at the fully discharged state. i) A schematic of the reaction mechanism for Cu₂S.

nanoporous arrays and binder-free traits not only supply ample space for alleviating strain during repeated cycles, but also emerge even greater virtue in furnishing high Mg²⁺/Li⁺ flux and continuous and fast conductive paths throughout electrode, enabling ultralong cycle life even in conversion cathode. Our scalable route would open up a novel direction for the rational design of binder-free material and hierarchical porous nano-architecture from an MOF precursor in enhancing the stability of conversion cathodes for applications.

4. Experimental Section

Synthesis of the Electrolyte: APC-based hybrid electrolyte was prepared according to reported method.^[7] All chemical preparations and experiments were performed in an argon-filled glove box (<0.1 ppm of oxygen and water). First, aluminum chloride (0.667 g, Aladdin, 99.9%) was slowly dissolved into THF (Sigma-Aldrich), followed by adding dropwise phenyl magnesium chloride (Macklin, 2 M solution in THF) under constant stirring and maintained for 12 h. At last, 1 M LiCl (Aladdin, 99.99%) was added under vigorous stirring and kept for another 12 h at room temperature.

In Situ Generation of Cu(OH)₂ Nanowire Arrays on CF: Prior to synthesis, a piece of CF (2 cm × 3 cm) was treated with HCl solution in an ultrasonic bath for 5 min to remove the oxide layer, and then ultrasonically washed with deionized water and ethanol for several times. Cu(OH)₂ nanowire arrays were prepared as follows. NaOH (25 mmol) and (NH₄)₂S₂O₈ (1.25 mmol) were respectively dissolved in two beakers with 10 mL deionized water. Then, 10 mL of NaOH solution was mixed with another 10 mL of (NH₄)₂S₂O₈ solution under vigorous stirring at room temperature. Subsequently, a piece of treated CF was immersed into above solution for consecutive 5 min at ambient temperature. After that, the resulting Cu(OH)₂ precursor was taken out and washed with water and ethanol several times, followed by drying at 60 °C under vacuum to obtain the blue Cu(OH)₂ nanowire arrays with a loading of ≈0.4 mg cm⁻².

Synthesis of Cu-MOF/CF: The Cu-MOF/CF was fabricated by a solvothermal method using above Cu(OH)₂/CF. Typically, PTA (0.133 mmol) was dissolved in DMF (30 mL), then continuous stirring for 20 min at room temperature. Then the above transparent solution and as-prepared Cu(OH)₂/CF were transferred into a 50 mL Teflon-lined stainless autoclave, which was sealed and maintained at 120 °C for 12 h. After cooling down to ambient temperature, the sample was taken out and washed with DMF several times, followed by drying at 60 °C under vacuum. The loading of Cu-MOF/CF was ≈3 mg cm⁻².

Synthesis of Cu₂S/CF, Cu₂S NW/CF, and Cu₂S HP/CF: The hierarchical Cu₂S nanoporous cluster arrays (Cu₂S HP/CF) was fabricated via

one-step thermal Cu-MOF-templated sulfuration based on solid-gas reaction. Typically, the resulting Cu-MOF precursor on CF and appropriate sulfur powder were put into two separate porcelain boats. After flushed with Ar, the center of the furnace was elevated to 300 °C at a ramping rate of 2 °C min⁻¹ and held at this temperature for 2 h, and then naturally cooled to ambient temperature under Ar. The mass loading for Cu₂S HP/CF was about 2.7 mg cm⁻². As comparison, Cu₂S/CF and Cu₂S NW/CF were made by varying Cu-MOF/CF to bare CF and Cu(OH)₂/CF, respectively, under otherwise identical experimental conditions used for preparing Cu₂S HP/CF. The mass loading for Cu₂S/CF and Cu₂S NW/CF were about 1.6 and 2.2 mg cm⁻², respectively.

Synthesis of Cu₂S HP Powder Electrode: Cu₂S HP powder was scraped down from Cu₂S HP/CF. The active material was prepared by coating slurries containing Cu₂S HP powder (70 wt%), Super P acetylene black (20 wt%), and polyvinylidene fluoride (10 wt%) on stainless steel. The mass loading of the electrodes was ≈0.8–1.0 mg cm⁻².

Characterizations: The phase structures were studied by XRD (D8 Advance, Bruker AXS) with Cu K α radiation and Jobin Yvon Horiba Raman spectrometer model HR800, with a 10 mW helium/neon laser at 632.8 nm excitation in the range of 100–2000 cm⁻¹. FTIR (Magna-IR 550 II, Nicolet) analysis was used to verify the functional groups in Cu-MOF and the composite. XPS was conducted on a Thermo Scientific K-Alpha spectrometer equipped with a monochromatic Al K α X-ray source (1486.6 eV) operating at 100 W. Samples were analyzed under vacuum ($P < 10^{-8}$ mbar) with a pass energy of 150 eV (survey scans) or 25 eV (high-resolution scans). All peaks would be calibrated with C1s peak binding energy at 284.8 eV for adventitious carbon. The morphology of the samples was analyzed using a field-emission SEM (JEOL7500FA, Tokyo, Japan). Elemental analysis was performed with an Elementar Vario EL3 elemental analyzer. Energy-filtered TEM (JEOL 2011 F, Tokyo, Japan) was used to investigate the microstructure and for elemental mapping. TGA (Netzsch STA 449 F3) connected to a mass spectrometer (MS, Hiden HPR 20) was carried out at a ramp rate of 10 °C min⁻¹ in air. Specific surface area determinations were performed using the BET method with an adsorption meter (Quadrasorb SI-MP). Porosity was determined by BJH/DH method. The ratio of Mg and Cu in the discharged cathode was analyzed by the ICP-MS (PerkinElmer NexION 300X).

Electrochemical Measurements: The electrochemical performances were measured with the use of 2032 coin-type cells in an argon-filled glove box. As-obtained materials were punched into a 12 mm disk as working electrodes. Magnesium metal and glass fiber were used as counter electrode and separator, respectively. APC-LiCl, which is widely used in magnesium-based hybrid batteries, was employed as electrolyte. In this work, the amount of electrolyte is ≈150 μ L per cell. Galvanostatic charge/discharge measurements were performed on a multichannel battery testing system within a potential range of 0.2–1.85 V versus Mg/Mg²⁺. CV was tested by a CHI 660D electrochemical workstation between 0.1–1.85 V versus Mg/Mg²⁺. EIS was also conducted using a CHI 660D electrochemical workstation. The amplitude was 10 mV, and the applied frequency range was from 100 kHz to 0.01 Hz. All of the tests were carried out at ambient temperature.

Supporting Information

Supporting Information is available from the Wiley Online Library or from the author.

Acknowledgements

This work was supported by in part the National Science Fund for Distinguished Young Scholars (51625102), the National Natural Science Foundation of China (51971065), and the Innovation Program of Shanghai Municipal Education Commission (2019-01-07-00-07-E00028).

Conflict of Interest

The authors declare no conflict of interest.

Data Availability Statement

Research data are not shared.

Keywords

binder-free cathodes, cuprous sulfide, hierarchical nanoporous arrays, hybrid magnesium-based batteries

Received: March 29, 2021

Revised: July 24, 2021

Published online: September 24, 2021

- [1] S. Chu, A. Majumdar, *Nature* **2012**, 488, 294.
- [2] B. Dunn, H. Kamath, J. M. Tarascon, *Science* **2011**, 334, 928.
- [3] H. D. Yoo, I. Shterenberg, Y. Gofer, G. Gershinsky, N. Pour, D. Aurbach, *Energy Environ. Sci.* **2013**, 6, 2265.
- [4] J. H. Cho, M. Aykol, S. Kim, J. H. Ha, C. Wolverton, K. Y. Chung, K. B. Kim, B. W. Cho, *J. Am. Chem. Soc.* **2014**, 136, 16116.
- [5] T. Gao, F. Han, Y. Zhu, L. Suo, C. Luo, K. Xu, C. Wang, *Adv. Energy Mater.* **2015**, 5, 1401507.
- [6] X. Fan, R. R. Gaddam, N. A. Kumar, X. S. Zhao, *Adv. Energy Mater.* **2017**, 7, 1700317.
- [7] R. Sun, C. Pei, J. Sheng, D. Wang, L. Wu, S. Liu, Q. An, L. Mai, *Energy Storage Mater.* **2018**, 12, 61.
- [8] J. Tian, D. Cao, X. Zhou, J. Hu, M. Huang, C. Li, *ACS Nano* **2018**, 12, 3424.
- [9] Z. Wang, G. Shao, *J. Mater. Chem. A* **2018**, 6, 6830.
- [10] D. Aurbach, Z. Lu, A. Schechter, Y. Gofer, H. Gizbar, R. Turgeman, Y. Cohen, M. Moshkovich, E. Levi, *Nature* **2000**, 407, 724.
- [11] C. Kim, P. J. Phillips, B. Key, T. Yi, D. Nordlund, Y. S. Yu, R. D. Bayliss, S. D. Han, M. He, Z. Zhang, A. K. Burrell, R. F. Klie, J. Cabana, *Adv. Mater.* **2015**, 27, 3377.
- [12] L. Luo, K. Zhou, R. Lian, Y. Lu, Y. Zhen, J. Wang, S. Mathur, Z. Hong, *Nano Energy* **2020**, 72, 104716.
- [13] T. Koketsu, J. Ma, B. J. Morgan, M. Body, C. Legein, W. Dachraoui, M. Giannini, A. Demortiere, M. Salanne, F. Dardoize, H. Groult, O. J. Borkiewicz, K. W. Chapman, P. Strasser, D. Dambournet, *Nat. Mater.* **2017**, 16, 1142.
- [14] Y. Wang, X. Xue, P. Liu, C. Wang, X. Yi, Y. Hu, L. Ma, G. Zhu, R. Chen, T. Chen, J. Ma, J. Liu, Z. Jin, *ACS Nano* **2018**, 12, 12492.
- [15] X. Sun, P. Bonnick, L. F. Nazar, *ACS Energy Lett.* **2016**, 1, 297.
- [16] Z. Wang, S. Rafai, C. Qiao, J. Jia, Y. Zhu, X. Ma, C. Cao, *ACS Appl. Mater. Interfaces* **2019**, 11, 7046.
- [17] Y. Shen, Y. Wang, Y. Miao, M. Yang, X. Zhao, X. Shen, *Adv. Mater.* **2020**, 32, 1905524.
- [18] W. Ren, F. Xiong, Y. Fan, Y. Xiong, Z. Jian, *ACS Appl. Mater. Interfaces* **2020**, 12, 10471.
- [19] D. He, D. Wu, J. Gao, X. Wu, X. Zeng, W. Ding, *J. Power Sources* **2015**, 294, 643.
- [20] F. Xiong, Y. Fan, S. Tan, L. Zhou, Y. Xu, C. Pei, Q. An, L. Mai, *Nano Energy* **2018**, 47, 210.
- [21] D. Chen, Y. Zhang, X. Li, J. Shen, Z. Chen, S.-a. Cao, T. Li, F. Xu, *Chem. Eng. J.* **2020**, 384, 123235.
- [22] X. Yao, J. Luo, Q. Dong, D. Wang, *Nano Energy* **2016**, 28, 440.
- [23] H. Tian, T. Gao, X. Li, X. Wang, C. Luo, X. Fan, C. Yang, L. Suo, Z. Ma, W. Han, C. Wang, *Nat. Commun.* **2017**, 8, 14083.

- [24] H. S. Kim, T. S. Arthur, G. D. Allred, J. Zajicek, J. G. Newman, A. E. Rodnyansky, A. G. Oliver, W. C. Boggess, J. Muldoon, *Nat. Commun.* **2011**, *2*, 427.
- [25] T. Gao, M. Noked, A. J. Pearse, E. Gillette, X. Fan, Y. Zhu, C. Luo, L. Suo, M. A. Schroeder, K. Xu, S. B. Lee, G. W. Rubloff, C. Wang, *J. Am. Chem. Soc.* **2015**, *137*, 12388.
- [26] A. Du, Z. Zhang, H. Qu, Z. Cui, L. Qiao, L. Wang, J. Chai, T. Lu, S. Dong, T. Dong, H. Xu, X. Zhou, G. Cui, *Energy Environ. Sci.* **2017**, *10*, 2616.
- [27] Z. Zhang, Z. Cui, L. Qiao, J. Guan, H. Xu, X. Wang, P. Hu, H. Du, S. Li, X. Zhou, S. Dong, Z. Liu, G. Cui, L. Chen, *Adv. Energy Mater.* **2017**, *7*, 1602055.
- [28] A. Du, Y. Zhao, Z. Zhang, S. Dong, Z. Cui, K. Tang, C. Lu, P. Han, X. Zhou, G. Cui, *Energy Storage Mater.* **2020**, *26*, 23.
- [29] G. Sai Gautam, P. Canepa, W. D. Richards, R. Malik, G. Ceder, *Nano Lett.* **2016**, *16*, 2426.
- [30] K. W. Nam, S. Kim, S. Lee, M. Salama, I. Shterenberg, Y. Gofer, J. S. Kim, E. Yang, C. S. Park, J. S. Kim, S. S. Lee, W. S. Chang, S. G. Doo, Y. N. Jo, Y. Jung, D. Aurbach, J. W. Choi, *Nano Lett.* **2015**, *15*, 4071.
- [31] M. Rashad, X. Li, H. Zhang, *ACS Appl. Mater. Interfaces* **2018**, *10*, 21313.
- [32] Y. Xu, W. Cao, Y. Yin, J. Sheng, Q. An, Q. Wei, W. Yang, L. Mai, *Nano Energy* **2019**, *55*, 526.
- [33] V. Soundharajan, B. Sambandam, S. Kim, V. Mathew, J. Jo, S. Kim, J. Lee, S. Islam, K. Kim, Y.-K. Sun, J. Kim, *ACS Energy Lett.* **2018**, *3*, 1998.
- [34] X. Lei, Y. Zheng, F. Zhang, Y. Wang, Y. Tang, *Energy Storage Mater.* **2020**, *30*, 34.
- [35] N. Wu, Z. Z. Yang, H. R. Yao, Y. X. Yin, L. Gu, Y. G. Guo, *Angew. Chem., Int. Ed.* **2015**, *54*, 5757.
- [36] P. Bonnick, X. Sun, K. C. Lau, C. Liao, L. F. Nazar, *J. Phys. Chem. Lett.* **2017**, *8*, 2253.
- [37] Z. Li, S. Ding, J. Yin, M. Zhang, C. Sun, A. Meng, *J. Power Sources* **2020**, *451*, 227815.
- [38] Y. Wang, Z. Liu, C. Wang, X. Yi, R. Chen, L. Ma, Y. Hu, G. Zhu, T. Chen, Z. Tie, J. Ma, J. Liu, Z. Jin, *Adv. Mater.* **2018**, *30*, 1802563.
- [39] Y. Wang, C. Wang, X. Yi, Y. Hu, L. Wang, L. Ma, G. Zhu, T. Chen, Z. Jin, *Energy Storage Mater.* **2019**, *23*, 741.
- [40] Q. Fu, A. Sarapulova, V. Trouillet, L. Zhu, F. Fauth, S. Mangold, E. Welter, S. Indris, M. Knapp, S. Dsoke, N. Bramnik, H. Ehrenberg, *J. Am. Chem. Soc.* **2019**, *141*, 2305.
- [41] C. Drosos, C. Jia, S. Mathew, R. G. Palgrave, B. Moss, A. Kafizas, D. Vernardou, *J. Power Sources* **2018**, *384*, 355.
- [42] R. Zhang, C. Ling, *ACS Appl. Mater. Interfaces* **2016**, *8*, 18018.
- [43] J. Cabana, L. Monconduit, D. Larcher, M. R. Palacin, *Adv. Mater.* **2010**, *22*, E170.
- [44] W. Wang, Y. Yang, Y. NuLi, J. Zhou, J. Yang, J. Wang, *J. Power Sources* **2020**, *445*, 227325.
- [45] Y. Zhang, Y. Li, Y. Wang, R. Guo, W. Liu, H. Pei, G. Yin, D. Ye, S. Yu, J. Xie, *J. Colloid Interface Sci.* **2019**, *553*, 239.
- [46] T. Li, A. Qin, H. Wang, M. Wu, Y. Zhang, Y. Zhang, D. Zhang, F. Xu, *Electrochim. Acta* **2018**, *263*, 168.
- [47] M. Mao, T. Gao, S. Hou, F. Wang, J. Chen, Z. Wei, X. Fan, X. Ji, J. Ma, C. Wang, *Nano Lett.* **2019**, *19*, 6665.
- [48] M. Wu, Y. Zhang, T. Li, Z. Chen, S. A. Cao, F. Xu, *Nanoscale* **2018**, *10*, 12526.
- [49] K. V. Kravchuk, R. Widmer, R. Erni, R. J. Dubey, F. Krumeich, M. V. Kovalenko, M. I. Bodnarchuk, *Sci. Rep.* **2019**, *9*, 7988.
- [50] J. Shen, Y. Zhang, D. Chen, X. Li, Z. Chen, S.-a. Cao, T. Li, F. Xu, *J. Mater. Chem. A* **2019**, *7*, 21410.
- [51] M. H. Ryou, J. Kim, I. Lee, S. Kim, Y. K. Jeong, S. Hong, J. H. Ryu, T. S. Kim, J. K. Park, H. Lee, J. W. Choi, *Adv. Mater.* **2013**, *25*, 1571.
- [52] B. Koo, H. Kim, Y. Cho, K. T. Lee, N. S. Choi, J. Cho, *Angew. Chem., Int. Ed.* **2012**, *51*, 8762.
- [53] I. Kovalenko, B. Zdyrko, A. Magasinski, B. Hertzberg, Z. Milicev, R. Burtovyy, I. Luzinov, G. Yushin, *Science* **2011**, *334*, 75.
- [54] S. Yuan, X. L. Huang, D. L. Ma, H. G. Wang, F. Z. Meng, X. B. Zhang, *Adv. Mater.* **2014**, *26*, 2273.
- [55] X. Cao, L. Cui, B. Liu, Y. Liu, D. Jia, W. Yang, J. M. Razal, J. Liu, *J. Mater. Chem. A* **2019**, *7*, 3815.
- [56] S. Wang, S. Jiao, J. Wang, H. S. Chen, D. Tian, H. Lei, D. N. Fang, *ACS Nano* **2017**, *11*, 469.
- [57] J. Gao, J. He, N. Wang, X. Li, Z. Yang, K. Wang, Y. Chen, Y. Zhang, C. Huang, *Chem. Eng. J.* **2019**, *373*, 660.
- [58] R. Sun, C. Pei, J. Sheng, D. Wang, L. Wu, S. Liu, Q. An, L. Mai, *Energy Storage Mater.* **2018**, *12*, 61.